Electrically induced strong modulation of magnon transport in ultrathin magnetic insulator films

J. Liu,[1] X-Y. Wei,[1,*] G. E. W. Bauer,[2,3] J. Ben Youssef,[4] and B. J. van Wees[1,†]

[1]*Physics of Nanodevices, Zernike Institute for Advanced Materials, University of Groningen, Nijenborgh 4, 9747 AG Groningen, The Netherlands*

[2]*Zernike Institute for Advanced Materials, University of Groningen, Nijenborgh 4, 9747 AG Groningen, The Netherlands*

[3]*WPI-AIMR & Institute for Materials Research & CSRN, Tohoku University, Sendai 980-8577, Japan*

[4]*LabSTICC, UMR CNRS 6285, Université de Bretagne Occidentale, 6 Avenue Le Gorgeu, 29238 Brest Cedex 3, France*

(Received 16 November 2020; revised 30 April 2021; accepted 25 May 2021; published 14 June 2021)

Magnon transport through a magnetic insulator can be controlled by current-biased heavy-metal gates that modulate the magnon conductivity via the magnon density. Here, we report nonlinear modulation effects in 10 nm thick yttrium iron garnet (YIG) films. The modulation efficiency is larger than 40%/mA. The spin-transport signal at high dc current density (2.2×10^{11} A/m^2) saturates for a 400 nm wide Pt gate, which indicates that even at high current levels a magnetic instability cannot be reached in spite of the high magnetic quality of the films.

DOI: 10.1103/PhysRevB.103.214425

I. INTRODUCTION

Magnons, i.e., the quanta of spin waves, are carriers of information with properties that are attractive for applications [1]. Magnons propagate in ferro-, ferri-, antiferro-, and even paramagnetic electric insulators without Joule heating [2–5]. The ferrimagnet yttrium iron garnet (YIG) is to date the best platform for magnon spintronics due to its low Gilbert damping and high Curie temperature. In YIG, magnons can be excited thermally and electrically and can cover long distances [6–8]. An electric current I in a thin-film platinum contact generates a spin accumulation at the Pt|YIG interface, which injects magnons into YIG. The latter diffuse into the magnet and generate a voltage V by the inverse spin Hall effect when reaching another Pt contact. The nonlocal resistance $R_{\rm nl} = V/I$ can be modulated by a third Pt film, as demonstrated for a 210 nm thick YIG film [9]. This three terminal device is a magnon transistor. The left and right ones inject and detect magnons thus form a *source* and a *drain*, respectively. Sending a current through the middle strip or *gate* modulates the source-drain signal by the magnon density in the transport channel; such structure is also available to study the magnon transport when the magnon gas is near Bose-Einstein condensation [10].

Chumak *et al.* [11] achieved magnon transistor action by controlling the magnon scattering in a magnonic crystal with a magnetic field. Our device operates by modulating the magnon conductivity of a YIG thin film $\sigma_{\rm m}$ electrically. Similar to the Drude formula for electrons, the magnon conductivity

$$\sigma_{\rm m} = \hbar \frac{n_{\rm m}\tau_{\rm m}}{m_{\rm m}}, \tag{1}$$

on the magnon density $n_{\rm m}$, where $\tau_{\rm m}$ is the scattering time and $m_{\rm m} = \hbar^2/(2J_{\rm s})$ is the effective mass that is governed by the spin-wave stiffness $J_{\rm s}$.

The present study is motivated by the wish to improve the modulation efficiency of the previous device [9]. This can be achieved simply by a thinner YIG film, since for the same number of injected magnons, the magnon density in the source-drain transport channel should be larger [12]. To this end we grew an ultrathin YIG film by liquid-phase epitaxy with thickness of 10 nm, so its Gilbert damping is as low as in thicker film. The observed modulation of the nonlocal signal reaches 200 % corresponding to a modulation efficiency per dc current unit exceed 40%/mA, which is 20 times larger than for the 210 nm YIG [9]. A similar enhancement has been reported for a 13 nm thick YIG film grown by pulsed laser deposition with larger Gilbert damping [12]. The authors interpret an observed nonlinearity in the gate-current dependence in terms of a diverging magnon conductivity by a spin Hall current-induced antidamping of the magnetization dynamics under the gate. Based on the observed dependence of the modulation on the gate width and geometry we believe that the physics is more complicated.

This paper is organized as follows: Section II addresses the device configuration, fabrication details and measurement methods. In Sec. III, we first compare the nonlocal signals in 10 nm and 210 nm thick YIG films. We then discuss the nonlinearities that in contrast to the previous report [12] saturate, discuss other device configurations, and show results of spin Hall magnetoresistance measurements of the Pt|YIG interface at high gate currents. In Sec. IV, we compare our results with those reported by Wimmer *et al.* [12].

II. EXPERIMENTAL DETAILS

The magnon transistors as depicted in Fig. 1 are fabricated on 10 nm thick single crystal yttrium iron garnet (YIG)

*x.wei@rug.nl
†b.j.van.wees@rug.nl

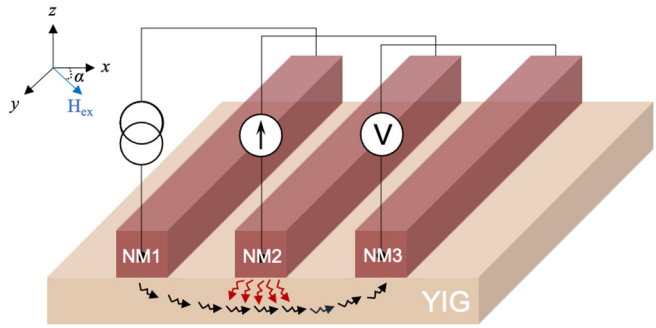

FIG. 1. Sample schematic**:** The sputtered Pt (red) strips with thickness of 9 nm are put on a 10 nm YIG film. A low-frequency ac current with rms value of I_{AC} in the left Pt strip injects magnons. We measure both the first and second harmonic voltages over the right Pt strip by a lock-in technique. The dc current through the middle Pt middle gate modulated the source-drain signal. An external magnetic field H_{ex} orients the in-plane YIG magnetization at an angle α. Typically, $\mu_0 H_{ex} = 50$ mT.

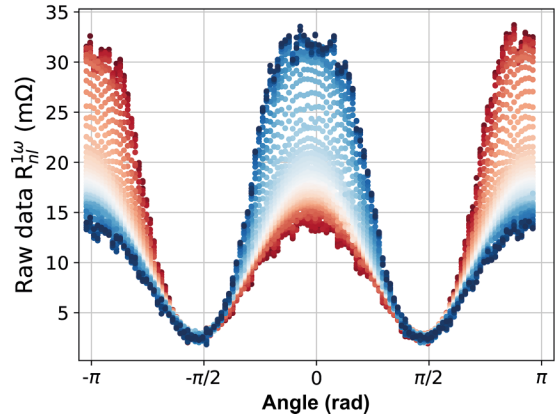

FIG. 2. Angle-dependent $R_{nl}^{1\omega}$ for Device 1 with injector/modulator/detector geometry**.** Raw data of the first harmonic signals $R_{nl}^{1\omega}$ at different dc gate currents with an offset from inductive/capacitive coupling (at $\alpha = \pm\pi/2$). The color gradient from red to blue represents dc currents from –1500 μA to +1500 μA with a step size of 50 μA.

films. The film is grown by liquid phase epitaxy (LPE) on top of a 500 μm thickness single crystal (110) gadolinium gallium garnet (GGG, $Gd_3Ga_5O_{12}$) substrate at the Université de Bretagne Occidentale in Brest, France. The saturation magnetization is $\mu_0 M_s = 174 \pm 4$ mT. The Gilbert damping parameter of the in-plane magnetized film is $\alpha_G = 5.2 \times 10^{-4}$. All Pt strips, including the magnon injector, modulator, and detector, are sputtered with thickness of 9 nm, patterned by electron beam lithography. Ti|Au layers with thicknesses of 5|75 nm are deposited by e-beam evaporation. The center-to-center distance between the injector and detector is 3 μm. The length and width of the Pt strips for 3 measured devices are listed in Table I, but we focus on Device 1. Results for a fourth device with 7.9 nm thickness YIG are summarized in Appendix B. The sample is positioned between a pair of magnetic poles and rotated by a step motor. The magnetic field $\mathbf{H}_{ex}$ orients the soft magnetization $\mathbf{M}_0 \| \mathbf{H}_{ex}$ in the film plane at an angle α with respect to the Pt strips as shown in Fig. 1.

A low-frequency (17.777 Hz) ac current passes through the magnon injector with an rms-amplitude of I_{AC}, thereby injecting magnons electrically and thermally. The resulting magnon spin currents are measured as the first and second harmonic signals at the magnon detector with a lock-in technique, respectively. A dc current I_{DC} is applied to the gate in order to modulate the magnon spin conductivity and the corresponding nonlocal signals.

The observed angle-dependent first harmonic signals of Device 1 are shown in Fig. 2: Colors, from red to blue code, represent the nonlocal signals recorded for I_{DC} from –1500 μA to +1500 μA. The white dataset in the center for $I_{DC} = 0$ has a typical $\cos^2\alpha$ dependence, i.e., the product of injection and detection efficiencies [8]. The dc bias modulates the magnitude and the angle dependence much more prominently than for a 210 nm thick YIG film [9], especially at the largest currents of $-/+1500$ μA (the darkest red/blue) and $\alpha \approx 0$ and $\alpha \approx \pm\pi$. The gate annihilates magnons in YIG when the spin accumulation is parallel to the magnetic field but creates them when antiparallel, suppressing, and enhancing $R_{nl}^{1\omega}$, respectively. The dc current enhances the signal by more than a factor of 2. Also the second harmonic signals are strongly modulated by the gate current (not shown), but more difficult to interpret since depending not only on the magnon density but also on the temperature profiles in the magnet. We therefore do not discuss them here.

TABLE I. Dimensions of the injector/modulator/detector Pt strips and selected observations. The centers of injectors and detectors are separated by 3 μm and the Pt film thicknesses is 9 nm in all samples.

Device	1	2	3
Length (μm)	80/84/80	20/24/20	20/24/20
Width (μm)	0.4/0.4/0.4	0.4/0.8/0.4	0.4/1.2/0.4
I_{AC} (μA)	200	500	500
I_{DC} (mA)	–1.5∼1.5	–2.0∼2.0	–2.25∼2.25
$R_{nl}^{1\omega}$ at $I_{DC} = 0$ (Ω/m)	198	1044	160
Modulation efficiency (%/mA)	40.4	87	75

III. RESULTS AND DISCUSSION

A. Dependence of the nonlocal signals on YIG film thickness

The nonlocal signals for 10 nm (Device 1 in Table I) and 210 nm thick YIG films with the same injector-to-detector distance (3 μm) are compared in Table II. The nonlocal resistances scale with the length of the Pt strips. The ultrathin gated but unbiased 10 nm YIG sample shows a larger nonlocal signal than the thick one without gate, even though a passive

TABLE II. Comparison of the first-harmonic nonlocal signals in 10 nm and 210 nm thick YIG films.

YIG thickness (nm)	10	210 (Ref. [8])
$R_{nl}^{1\omega}$ (Ω m^{-1})	198	140
$R_{nl}^{2\omega}$ (MVA^{-2} m^{-1})	0.09	1.35

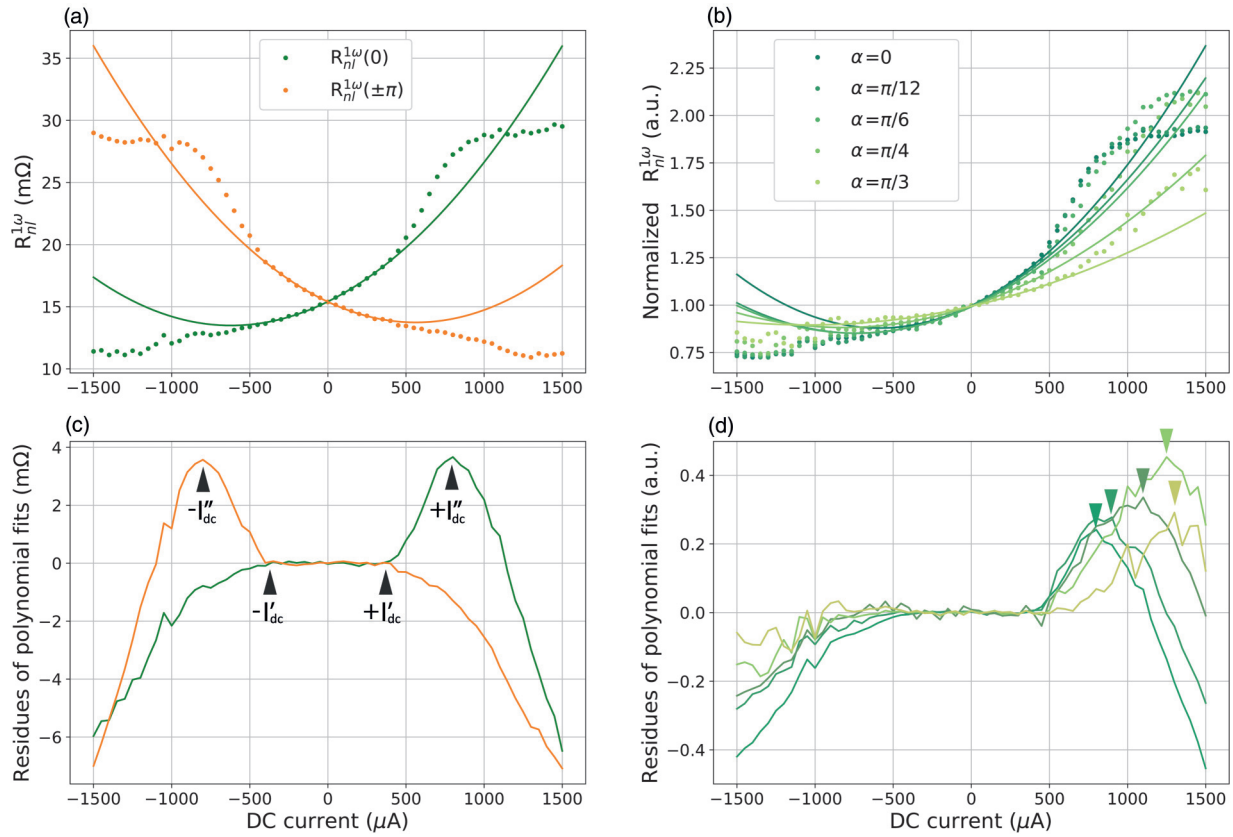

FIG. 3. Analysis of $R_{nl}^{1\omega}$ at specific angles α for Device 1 with injector/modulator/detector geometry. The dots are the experimental data and the lines with the same color are quadratic fits for small currents. (a) • $R_{nl}^{1\omega}(0)$ and $\alpha + \phi^{1\omega} = \pm\pi$ [• $R_{nl}^{1\omega}(\pm\pi)$] as a function of dc gate current I_{DC}. (b) Data for $\alpha = \{0, \pi/12, \pi/6, \pi/4, \pi/3\}$ normalized by the amplitudes at $I_{DC} = 0$ (green dots with different brightness). The deviations from the fits in (a) and (b) are plotted in (c) and (d), respectively.

central gate is a spin sink. This result is consistent with the thickness-dependence reported for films from 100 nm up to 50 μm [13], but counterintuitive since a thinner film should have a higher impedance. It cannot be explained by either the magnon chemical potential model [14] nor viscous magnon flow [15]. On the other hand, the second harmonic spin Seebeck signal in 10 nm thick YIG (not shown) is much smaller in the 10 nm than in the 210-nm film. The thickness dependence of the nonlocal magnon transport remains unexplained. We may speculate for example about the existence of highly efficient surface transport channels that dominate in ultrathin films. The thickness dependence of the nonlocal signal will be discussed in a future paper with more details.

B. Saturation in the injector/modulator/detector geometry for a 400 nm wide gate

The nonlocal resistances $R_{nl}^{1\omega}$ are trigonometric functions of the magnetic field angle α that reflect the electrical magnon injection and detection efficiencies [8]. The angle-dependent first-harmonic nonlocal resistances are well described by

$$R_{nl}^{1\omega}(\alpha) = C_1 \sigma_m^{1\omega}(\alpha) \cos^2 \alpha, \tag{2}$$

where C_1 is a charge-spin conversion efficiency parameter of the electric spin injection and detection. In the limit of weak excitation, the magnon spin conductivity depends linearly on the magnon density which is again proportional to the direction and the amplitude of injected current. We also include a quadratic term that does not depend on the current direction and is caused by Joule heating. Hence

$$\sigma_m^{1\omega}(\alpha) = \sigma_m^0 + \Delta\sigma_{SHE} I_{DC} \cos\alpha + \Delta\sigma_J I_{DC}^2, \tag{3}$$

where I_{DC} is the dc current in the modulator, σ_m^0 is the magnon spin conductivity at thermal equilibrium, $\Delta\sigma_J$ and $\Delta\sigma_{SHE}$ are parameters that can be fitted to the observations.

We extract the nonlocal resistances at specific angles from Fig. 2 as a function of I_{DC}, subtracting a constant offset at $\alpha = \pm\pi/2$ from the measured $R_{nl}^{1\omega}(\alpha)$ that is caused by inductive/capacitive coupling. The signals at the angles $\alpha = 0, \pm\pi$ are shown in Fig. 3(a) as well as normalized ones for $\alpha = 0, \frac{\pi}{12}, \frac{\pi}{6}, \frac{\pi}{4}$, and $\frac{\pi}{3}$ in Fig. 3(b). When $|I_{DC}| < I'_{DC} = 400\,\mu$A (the current density is 1.1×10^{11} A/m^2), $R_{nl}^{1\omega}(\alpha)$ in Fig. 3(a) is to a good approximation a parabolic function of I_{DC} :

$$R_{nl}^{1\omega}(I_{DC}) = \mathcal{P}_0^{1\omega} + \mathcal{P}_1^{1\omega} I_{DC} + \mathcal{P}_2^{1\omega} I_{DC}^2, \tag{4}$$

with $\mathcal{P}_1^{1\omega} \sim 6\,\Omega$/A and $\mathcal{P}_2^{1\omega} \sim 5 \times 10^3\,\Omega$/A^2 [$\mathcal{P}_0^{1\omega} = 1$ for the normalized data in Fig. 3(b)]. The differences between the observations and the fits of Figs. 3(a) and 3(b) are given in Figs. 3(c) and 3(d), respectively. The data deviates from the fits at the first threshold current $|I_{DC}| \gtrsim I'_{DC} = 400\,\mu$A (current density 1.1×10^{11} A/m^2). At a second threshold $I''_{DC} = 800\,\mu$A (current density 2.2×10^{11} A/m^2) the deviations from the polynomial fits show a *maximum* that we call

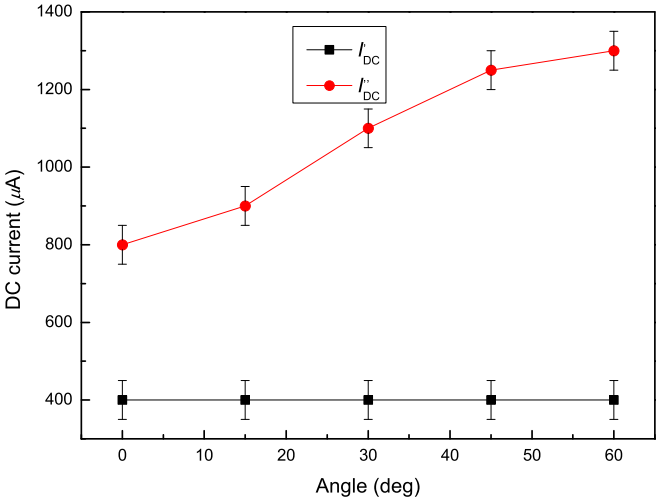

FIG. 4. I'_{DC} and I''_{DC} vs angle α in Device 1 with injector/modulator/detector geometry.

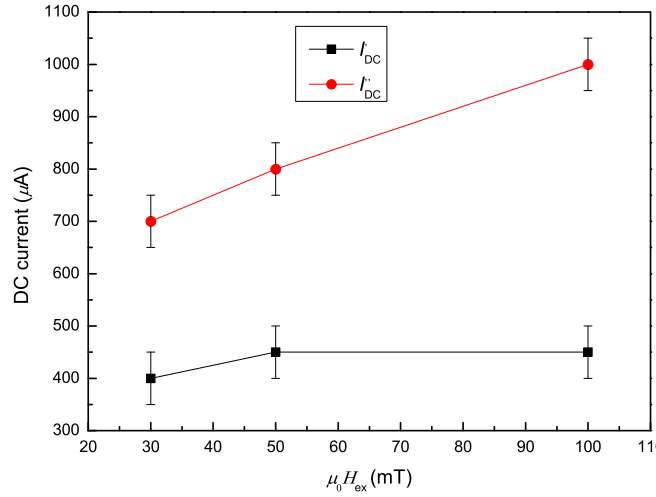

FIG. 6. I'_{DC} and I''_{DC} vs magnetic field strength in Device 1 with injector/modulator/detector geometry.

an *anomaly* for convenience. For $I_{DC} < 0$ the parabolic model Eq. (3) predicts an increase of the magnon conductivity by the parabolic term that models the magnon injection by Joule heating. However, $R^{1\omega}_{nl}(0)$ deviates from this prediction for $I_{DC} \lesssim -I'_{DC}$, i.e., at the same current level as for positive gate currents. The experiments confirm that reversing the magnetic field is equivalent to reversing the current direction. In Fig. 4, the threshold I''_{DC} increases with the angle α, while I'_{DC} remains constant. Since with increasing α a higher current is required to inject the same number of magnons, I''_{DC} appears to be related with the magnon injection process, while I'_{DC} is not.

For the injector/modulator/detector geometry here, the threshold current I'_{DC} separates the low and high dc current regimes. The enhancement of the magnon transport at currents $I > I'_{DC}$ indicates interesting physics such as current-induced self-oscillations of the magnetic order. However, instead of a divergence that could indicate magnon superfluidity, we observe a plateau at high-current levels [see Fig. 3(a)].

The differences between the data and a parabolic fit at low injection currents give us some clues about what is happening underneath the Pt. We clearly observe nonparabolicities for both positive and negative currents, i.e., for both magnon injection and extraction. At $I > I'_{DC}$ the signal is enhanced, i.e., increases above the parabolic fit. This threshold is not sensitive to the direction of applied magnetic fields, which indicates a thermal (spin Seebeck) mechanism for the enhancement of the conductivity as reported by Safranski *et al.* [16].

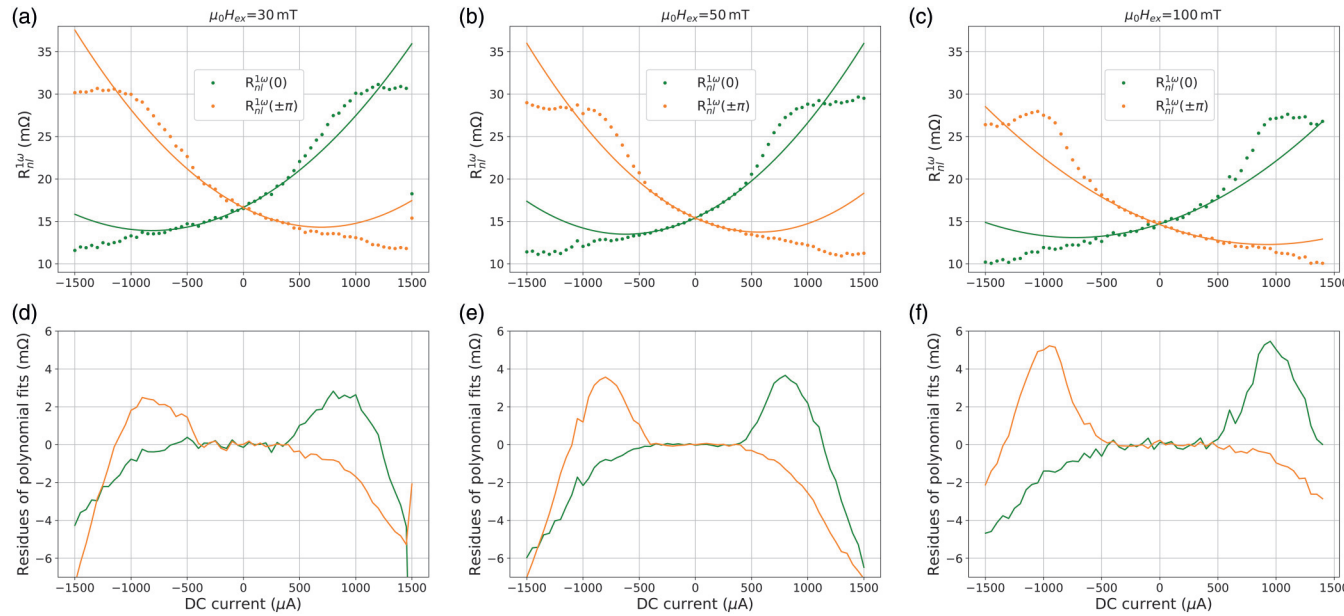

FIG. 5. Analysis of the nonparabolicties in $R^{1\omega}_{nl}$ of Device 1 for different magnetic field with injector/modulator/detector geometry. We plot the deviations from the small-field parabolic fits for $\alpha = 0$ [$\bullet R^{1\omega}_{nl}(0)$] and $\alpha = \pm\pi$ [$\bullet R^{1\omega}_{nl}(\pm\pi)$] as a function of the modulator current I_{DC} at 30 mT, (b) 50 mT, and (c) 100 mT.

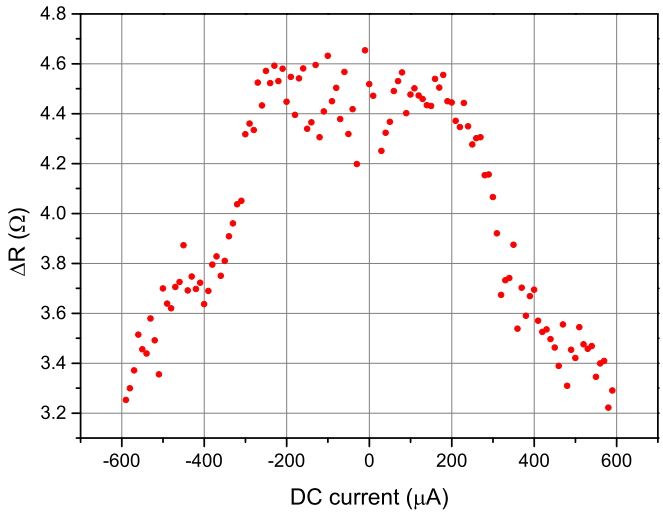

FIG. 7. (Longitudinal) spin Hall magnetoresistance of the 400-nm wide central Pt gate at dc current from −590 μA to 590 μA.

C. External field dependence of the saturation

A field-dependent study in Fig. 5 can shed light on the possible effect of the magnon gap or Kittel frequency

$$\omega_{k=0} = \gamma\sqrt{B_0(B_0 + \mu_0 M_s)}, \tag{5}$$

on the anomaly I''_{DC}. The results in Fig. 6 show a slightly increased I''_{DC} with field from 700 μA to 1 mA. I'_{DC}, which does not depend on the magnetization angle above, remains also resilient against the magnetic field strength. Although we cannot pinpoint the process that suppresses the magnon conduction at high current levels to a certain mechanism, but it appears to be spin-dependent since in contrast to I'_{DC}, I''_{DC} depends strongly on the magnetic field strength and direction. This could reflect a gap-induced reduction of the magnon number and conductivity.

D. Spin Hall magnetoresistance of the 400 nm wide Pt strip

Next, we analyze the spin Hall magnetoresistance (SMR) of the 400 nm wide Pt center gate [17] for an ac current of 20 μA and a dc current range from –590 μA to 590 μA. Fig. 7 shows that the resistance change ΔR decreases when increasing dc current I_{DC} with a threshold around ±400 μA, which is close to I'_{DC} introduced above. The SMR decreases with the temperature [18] and appears to be correlated with I'_{DC}, the first threshold in the nonlocal signal, thereby it support the hypothesis that Joule heating affects the spin-transport at the interface. It is consistent with the independence of I'_{DC}, on the magnetic field reported above.

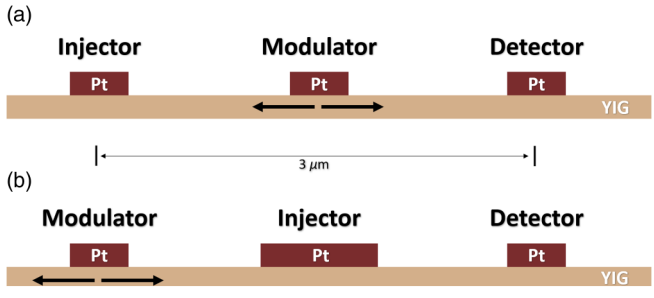

FIG. 8. Positions of the modulating gate in (a) Sample 1 and (b) Sample 2. The black arrows represent the magnon diffusion currents injected by the modulator. The density of magnons between injector and detector and therefore gate efficiency should be smaller in (b) (see discussion in the text). The distance between the centers of the outer Pt contacts is 3 μm.

TABLE III. Geometry of modulator/injector/detector Pt strips and measurement parameters on Device 2.

Length (μm)	20/24/20
Width (μm)	0.4/0.8/0.4
Pt thickness (nm)	9
I_{AC} (μA)	500
I_{DC} (mA)	–1.6∼1.7
Modulation efficiency (%/mA)	23.5

E. Exchanged source and gate contacts

In order to collect more information on the anomalies observed in Fig. 3 we exchange roles of the Pt contacts from an injector/modulator/detector to a modulator/injector/detector geometry as sketched in Figs. 8(b) and specified in Table III. In this configuration the source-drain current is not directly affected by an antidamping torque of the modulator. The signal is larger because the injector and detector are now closer to each other. The first harmonic signal for the new configuration in Fig. 9 is well represented by a parabola with $\mathcal{P}_1^{1\omega} \sim 1.6 \times 10^{-2}\,\Omega/\mathrm{A}$ and $\mathcal{P}_2^{1\omega} \sim 18\,\Omega/\mathrm{A}^2$ in Eq. (4) for $|I_{DC}| < I'_{DC} = 900\,\mu$A. $R_{nl}^{1\omega}(0)$ $[R_{nl}^{1\omega}(\pm\pi)]$ starts to decrease for at currents $I_{DC} = 900\,\mu$A (1400 μA) and $I_{DC} = -1400\,\mu$A (–900 μA). In contrast to the discussion above, the deviations from the parabolic fit at I'_{DC} are negative so we cannot identify a I''_{DC}.

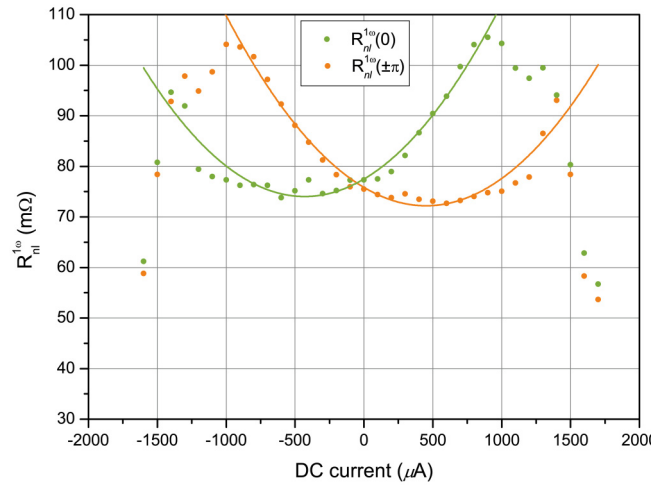

FIG. 9. Analysis of $R_{nl}^{1\omega}$ at specific angles for modulator/injector/detector configuration of Device 2. Relative amplitudes of the first harmonic nonlocal signals of device 2 with 800 nm width modulator at $\alpha = 0$ [$\bullet R_{nl}^{1\omega}(0)$] and $\alpha = \pm\pi$ [$\bullet R_{nl}^{1\omega}(\pm\pi)$] as a function of dc currents.

In the modulator/injector/detector geometry, magnons injected by the modulator first have to diffuse to the source-drain channel in order to affect the magnon conductivity. The magnon chemical potential μ_m is a direct measure of the nonequilibrium magnon density that obeys the spin-diffusion equation $d^2\mu_m/dx^2 = \mu_m/\lambda_m^2$ [8] with a magnon diffusion length of $\lambda_m \sim 10\,\mu$m at room temperature. Here, due to the diffusion of magnons and the absorption by the wider injector, the loss of dc-injected magnon density in the source-drain channel is much more than 20% comparing to the center gate configuration with the same dc current passing though the modulator. Therefore, a larger current is required to achieve the same magnon density.

When the modulator is in the center, the magnon transmission is affected by thermal [19,20] or electric [21,22] spin-orbit torques as well as spin absorption by the Pt gate. The situation is simplified for the modulator/injector/detector geometry in so far that the modulator is only a source of additional magnons that increase the injector-detector conductance. I'_{DC} is larger for this configuration, presumably because the higher current level is required to generate the same density in the source-drain channel by magnon diffusion.

F. Modulator gate width dependence

In Device 2 (800-nm wide modulator) and Device 3 (1200 nm wide modulator) from Table I (see Fig. 10), a saturation as in Device 1 [Fig. 3(a)] is not observed. The characteristics are similar to that of Device 1 in the modulator/injector/detector configuration: $R_{nl}^{1\omega}$ deviates from the simple magnon conductivity model at lower currents. Device 2 deviates at currents (current densities) of 500 μA (0.7×10^{11} A/m^2) and starts to decrease at 1 mA (1.4×10^{11} A/m^2). Device 3 deviates from 0.6×10^{11} A/m^2 and starts to decrease at 1.2×10^{11} A/m^2. They are much lower than the current density corresponding to the saturation in Device 1 (2.2×10^{11} A/m^2). Naively, we expected that for equal current densities the results should not depend on the width of the gate. Nevertheless, we find that widening the central gates only decreases the signals relative to the polynomial fit. A proper explanation of this result requires more research.

We also observe signal changes induced by a high dc current bias on Device 3 (see Appendix A) that indicate a transient change of the magnetic order of the YIG film that may also cause the asymmetry between the data in Fig. 10(b) for flipped current and magnetization directions. We observed a strong increase of the nonlocal signals in Device 3 after we removed the dc current. Since we have not been able to explain or repeat these results, we do not discuss them in the main text.

IV. CONCLUSIONS

We observe a threshold behavior at currents $I > I'_{DC}$ that indicates that the film under the gate approaches an instability, confirming previous reports. The threshold does not depend on the magnetization direction and therefore the spin Hall

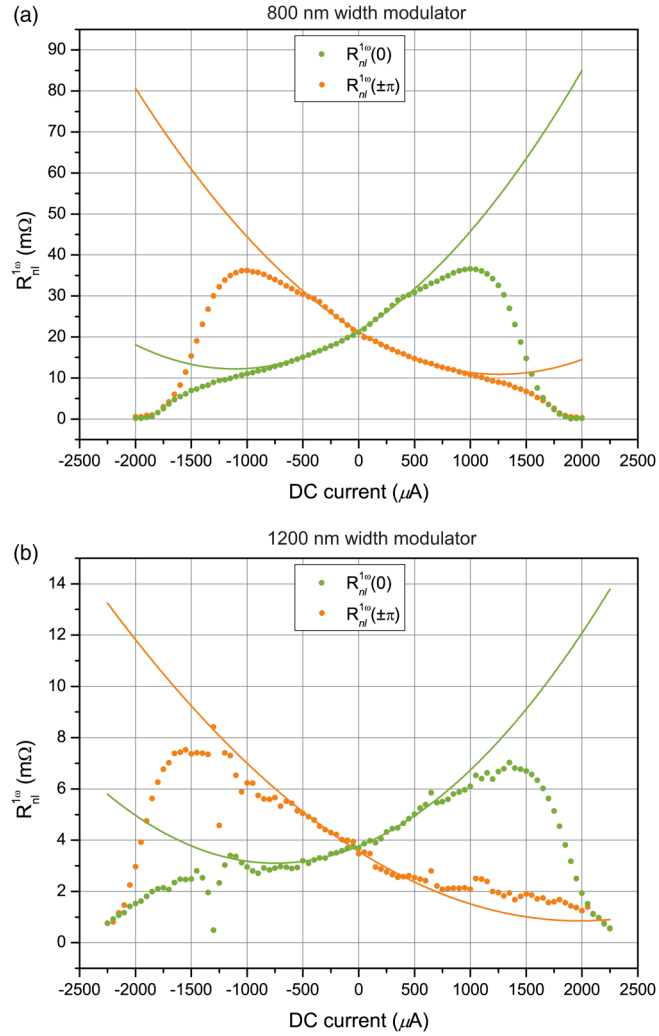

FIG. 10. $R_{nl}^{1\omega}$ for Devices 2 and 3 with wider modulator gates as a function of gate current I_{DC} in injector/modulator/detector geometry. (a) The signals of Device 2 with 800 nm wide modulator at $\alpha = 0$ [$\bullet R_{nl}^{1\omega}(0)$] and $\alpha = \pm\pi$ [$\bullet$ $R_{nl}^{1\omega}(\pm\pi)$] as a function of dc currents. (b) As a function of gate current I_{DC}, but for Device 3 with 1200 nm wide modulator.

injection, which could indicate an enhancement of the magnon density by the spin Seebeck effect. However, at negative currents the magnon accumulation remains suppressed which indicates that the spin Hall effect injection dominates the spin Seebeck effect. At even higher currents $I \gtrsim I''_{DC}$ another effect kicks in that suppresses the magnon density and conductivity again. This process is roughly symmetric in the current direction and may be assigned to a nonlinear magnon decay into phonons at elevated temperatures.

Wimmer *et al.* [12] also report nonlinear effects induced by a Pt gate current on magnon transport. Their sample is slightly thicker with 13.5 nm with a damping of $\alpha_G = 2.17 \times 10^{-3}$, which is significantly higher than our $\alpha_G = 5.2 \times 10^{-4}$. They report two anomalies (I_{on} and I_{crit}). The first appears to agree with our I'_{DC} and results for $I_{DC} < I'_{DC}$ agree qualitatively with our data and the magnon conductivity Eq. (3). The current densities corresponding

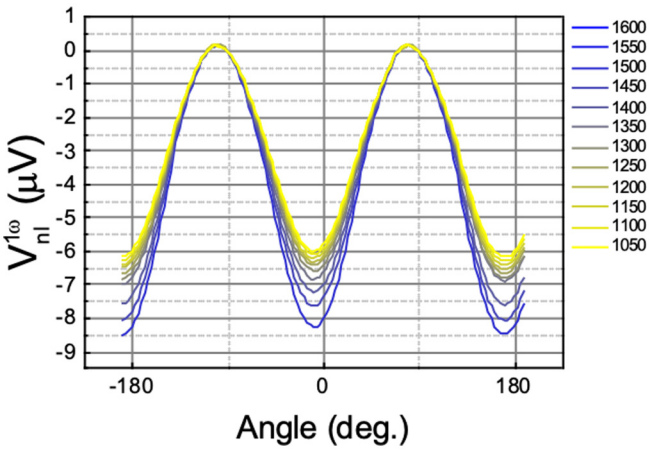

FIG. 11. Angle-dependent first harmonic voltages at high gate current levels on Device 3 with injector/modulator/detector geometry. The nonlocal signal continues to increase with increasing current.

to I_{on} (3.2×10^{11} A/m^2) and I_{crit} (4.3×10^{11} A/m^2) are much higher than our I'_{DC} (1.1×10^{11} A/m^2) and I''_{DC} (2.2×10^{11} A/m^2). They do not report transport for opposite gate current direction and the associated suppression of the nonlocal signals, however. For $I_{DC} > I_{on}$, Wimmer *et al.* [12] observe signals that increases faster than the parabolic fit, which we confirm here. However, they do not find the saturation we report in Fig. 3(a). Wimmer *et al.* [12] interpret the monotonic increase of their results as an incipient divergence by an anti-damping spin-orbit torque that compensates the damping in the YIG film under the gate and speculate about lossless magnon transport at the onset of self-oscillations or superfluidity. On the other hand, the larger Gilbert damping in their samples could imply that the magnon densities at their highest current levels is significantly lower than ours, so they do not reach the saturation regime that we report here.

Concluding, before drawing conclusion about the nature of nonlinearities, the complications due to heating should be figured out in more detail [23–26]. It would be valuable to assess the magnon spin accumulation profile governed by the temperature gradient [27], which may be different in thin and thick films. We conclude that ultrathin YIG films are a great platform for the research on magnon transport in nonlinear regime, but much work has still to be carried out before magnon Bose-Einstein condensation or superfluidity by electric or thermal spin injection can be confirmed.

ACKNOWLEDGMENTS

We acknowledge the helpful discussion with T. Yu and technical support from J. G. Holstein, H. M. de Roosz, H. Adema, T. Schouten, and H. de Vries. This work is part of the research program Magnon Spintronics (MSP) No. 159 financed by the Foundation for Fundamental Research on Matter (FOM), which is part of the Nederlandse Organisatie voor Wetenschappelijk Onderzoek (NWO), and supported by the research programme Skyrmionics with project number 170, which is financed by the Nederlandse Organisatie voor Wetenschappelijk Onderzoek (NWO). The support by NanoLab NL the Spinoza Prize awarded in 2016 to B.J.v.W. by NWO is also gratefully acknowledged. G.B. was supported by JSPS Kakenhi Grant No. 19H00645.

APPENDIX A: SIGNAL CHANGE AFTER GATE MEASUREMENT

Device 3 underwent a transient change after applying a high dc current to the gate. The signal became symmetric around zero angle and enhanced for both 0 and 180 degrees, see Fig. 11, indicating an unidentified thermal mechanism. After this experiment, the nonlocal signal at zero gate current increased by a factor five as shown in Fig. 12. The high dc current appeared to change the properties of YIG under the gate. However, after about two weeks, the characteristics of Device 3 returned back to normal as shown in Fig. 10(b).

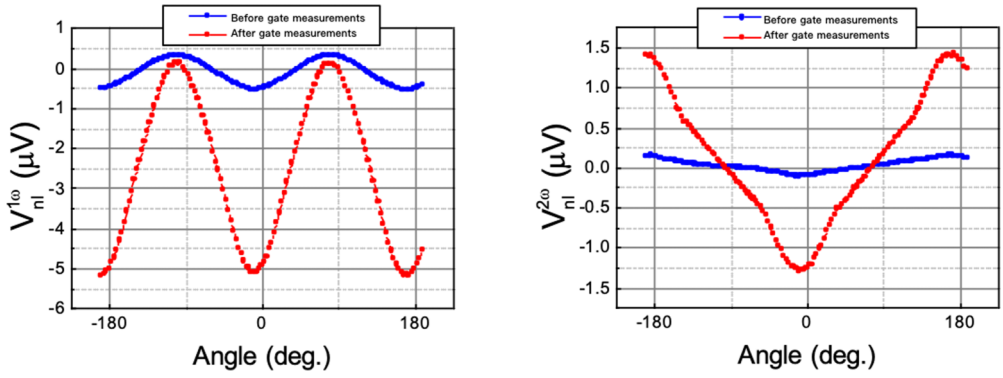

FIG. 12. Angle-dependent nonlocal magnon transport measurement before and after a measurement at high gate currents on Device 3 with injector/modulator/detector geometry. The heating that accompanies a large current changes the properties of YIG. (a) Angle-dependent first harmonic voltage before and after the gate-induced heating at zero gate current. (b) Angle-dependent second harmonic measurement before and after. Both first- and second-harmonic signals are strongly enhanced after the heating. However, the effect appears to be transient and could not be reproduced.

TABLE IV. Geometry of injector/modulator/detector Pt strips.

Length (μm)	20/25/20
Width (μm)	0.4/0.4/0.4
Pt thickness (nm)	8
I_{AC} (μA)	200
I_{DC} (mA)	–1.75∼1.75
Distance between centers of Pt (μm)	1.5

APPENDIX B: MODULATION EFFECT ON 7.9 nm THICK YIG

We also study a transistor structure on a 7.9 nm thick YIG with damping parameter of $\alpha_G = 6.3 \times 10^{-4}$. The device parameters are shown in Table IV. Compared to the 10-nm thick YIG, we observe in Fig. 13 a modulation increased by a factor of 3 instead of 2. We have to apply a higher dc currents to reach the nonlinear regime but still observe a saturation at the highest currents.

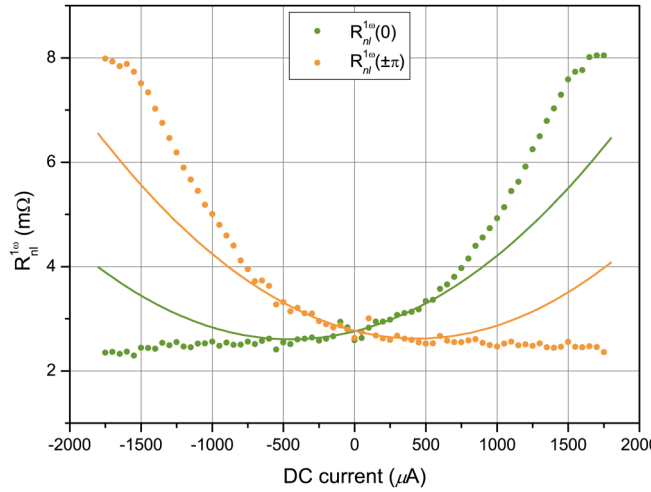

FIG. 13. $R_{nl}^{1\omega}$ for injector/modulator/detector configuration for the 7.9-nm YIG film specified in Table IV. Relative amplitudes of the first harmonic nonlocal signals of device 2 with 800 nm width modulator at $\alpha = 0$ [$\bullet R_{nl}^{1\omega}(0)$] and $\alpha = \pm\pi$ [$\bullet R_{nl}^{1\omega}(\pm\pi)$] as a function of dc currents.

[1] A. V. Chumak, V. I. Vasyuchka, A. A. Serga, and B. Hillebrands, Nat. Phys. **11**, 453 (2015).
[2] C. Kittel, Phys. Rev. **110**, 1295 (1958).
[3] J. R. Eshbach, Phys. Rev. Lett. **8**, 357 (1962).
[4] R. Lebrun, A. Ross, S. A. Bender, A. Qaiumzadeh, L. Baldrati, J. Cramer, A. Brataas, R. A. Duine, and M. Kläui, Nature (London) **561**, 222 (2018).
[5] K. Oyanagi, S. Takahashi, L. J. Cornelissen, J. Shan, S. Daimon, T. Kikkawa, G. E. W. Bauer, B. J. van Wees, and E. Saitoh, Nat. Commun. **10**, 4740 (2019).
[6] K. Uchida, S. Takahashi, K. Harii, J. Ieda, W. Koshibae, K. Ando, S. Maekawa, and E. Saitoh, Nature (London) **455**, 778 (2008).
[7] Y. Kajiwara, K. Harii, S. Takahashi, J. Ohe, K. Uchida, M. Mizuguchi, H. Umezawa, H. Kawai, K. Ando, K. Takanashi, S. Maekawa, and E. Saitoh, Nature (London) **464**, 262 (2010).
[8] L. J. Cornelissen, J. Liu, R. A. Duine, J. Ben Youssef, and B. J. van Wees, Nat. Phys. **11**, 1022 (2015).
[9] L. J. Cornelissen, J. Liu, B. J. van Wees, and R. A. Duine, Phys. Rev. Lett. **120**, 097702 (2018).
[10] S. Takei, Phys. Rev. B **100**, 134440 (2019).
[11] A. V. Chumak, A. A. Serga, and B. Hillebrands, Nat. Commun. **5**, 4700 (2014).
[12] T. Wimmer, M. Althammer, L. Liensberger, N. Vlietstra, S. Geprägs, M. Weiler, R. Gross, and H. Huebl, Phys. Rev. Lett. **123**, 257201 (2019).
[13] J. Shan, L. J. Cornelissen, N. Vlietstra, J. Ben Youssef, T. Kuschel, R. A. Duine, and B. J. van Wees, Phys. Rev. B **94**, 174437 (2016).
[14] L. J. Cornelissen, K. J. H. Peters, G. E. W. Bauer, R. A. Duine, and B. J. van Wees, Phys. Rev. B **94**, 014412 (2016).
[15] C. Ulloa, A. Tomadin, J. Shan, M. Polini, B. J. van Wees, and R. A. Duine, Phys. Rev. Lett. **123**, 117203 (2019).
[16] C. Safranski, I. Barsukov, H. K. Lee, T. Schneider, A. A. Jara, A. Smith, H. Chang, K. Lenz, J. Lindner, Y. Tserkovnyak, M. Wu, and I. N. Krivorotov, Nat. Commun. **8**, 117 (2017).
[17] Y. Chen, D. Roy, E. Cogulu, H. Chang, M. Wu, and A. D. Kent, Appl. Phys. Lett. **113**, 202403 (2018).
[18] S. Vélez, A. Bedoya-Pinto, W. Yan, L. E. Hueso, and F. Casanova, Phys. Rev. B **94**, 174405 (2016).
[19] E. Padrón-Hernández, A. Azevedo, and S. M. Rezende, Phys. Rev. Lett. **107**, 197203 (2011).
[20] S. A. Bender and Y. Tserkovnyak, Phys. Rev. B **93**, 064418 (2016).
[21] A. Hamadeh, O. d'Allivy Kelly, C. Hahn, H. Meley, R. Bernard, A. H. Molpeceres, V. V. Naletov, M. Viret, A. Anane, V. Cros, S. O. Demokritov, J. L. Prieto, M. Muñoz, G. de Loubens, and O. Klein, Phys. Rev. Lett. **113**, 197203 (2014).
[22] M. Collet, X. de Milly, O. d'Allivy Kelly, V. V. Naletov, R. Bernard, P. Bortolotti, J. Ben Youssef, V. E. Demidov, S. O. Demokritov, J. L. Prieto, M. Muñoz, V. Cros, A. Anane, G. de Loubens, and O. Klein, Nat. Commun. **7**, 10377 (2016).
[23] N. Thiery, V. V. Naletov, L. Vila, A. Marty, A. Brenac, J.-F. Jacquot, G. de Loubens, M. Viret, A. Anane, V. Cros, J. Ben Youssef, N. Beaulieu, V. E. Demidov, B. Divinskiy, S. O. Demokritov, and O. Klein, Phys. Rev. B **97**, 064422 (2018).
[24] H. J. Qin, K. Zakeri, A. Ernst, and J. Kirschner, Phys. Rev. Lett. **118**, 127203 (2017).
[25] S. Geprägs, A. Kehlberger, F. D. Coletta, Z. Qiu, E.-J. Guo, T. Schulz, C. Mix, S. Meyer, A. Kamra, M. Althammer, H. Huebl, G. Jakob, Y. Ohnuma, H. Adachi, J. Barker, S. Maekawa, G. E. W. Bauer, E. Saitoh, R. Gross, S. T. B. Goennenwein *et al.*, Nat. Commun. **7**, 10452 (2016).
[26] Y. Nambu, J. Barker, Y. Okino, T. Kikkawa, Y. Shiomi, M. Enderle, T. Weber, B. Winn, M. Graves-Brook, J. M. Tranquada, T. Ziman, M. Fujita, G. E. W. Bauer, E. Saitoh, and K. Kakurai, Phys. Rev. Lett. **125**, 027201 (2020).
[27] J. Shan, L. J. Cornelissen, J. Liu, J. Ben Youssef, L. Liang, and B. J. van Wees, Phys. Rev. B **96**, 184427 (2017).